Earth and Planetary Science Letters 553 (2021) 116641

Contents lists available at ScienceDirect

Earth and Planetary Science Letters

www.elsevier.com/locate/epsl

The role of fluid chemistry on permeability evolution in granite: Applications to natural and anthropogenic systems

C. Sanchez-Roa [a,*], G.D. Saldi [a], T.M. Mitchell [a], F. Iacoviello [b], J. Bailey [b], P.R. Shearing [b], E.H. Oelkers [a,c], P.G. Meredith [a], A.P. Jones [a], A. Striolo [d]

[a] Department of Earth Sciences, University College London, London, WC1E 6BT, UK
[b] Electrochemical Innovation Lab, Department of Chemical Engineering, University College London, London, WC1E 6BT, UK
[c] Géosciences Environnement Toulouse (GET), CNRS, UMR 5563, Observatoire Midi-Pyrénées, 14 Ave. E. Belin, 31400 Toulouse, France
[d] Department of Chemical Engineering, University College London, London, WC1E 6BT, UK

ARTICLE INFO

Article history:
Received 13 March 2020
Received in revised form 7 August 2020
Accepted 13 October 2020
Available online 6 November 2020
Editor: H. Handley

Keywords:
permeability
fluid-rock interaction
dissolution
clay mineral precipitation
geothermal systems

ABSTRACT

Efforts to maintain and enhance reservoir permeability in geothermal systems can contribute to sourcing more sustainable energy, and hence to lowering CO_2 emissions. The evolution of permeability in geothermal reservoirs is strongly affected by interactions between the host rock and the fluids flowing through the rock's permeable pathways. Precipitation of secondary mineral phases, the products of fluid-rock interactions, within the fracture network can significantly reduce the permeability of the overall system, whereas mineral dissolution can enhance reservoir permeability. The coupling between these two competing processes dictates the long-term productivity and lifetime of geothermal reservoirs. In this study, we simulate the conditions within a geothermal system from induced fracturing to the final precipitation stage. We performed batch and flow-through experiments on cores of the Carnmenellis granite, a target unit for geothermal energy recovery in Cornwall (UK), to understand the role of mineral dissolution and precipitation in controlling the permeability evolution of the system. The physico-chemical properties of the cores were monitored after each reaction-phase using ICP-OES, SEM, hydrostatic permeability measurements, and X-ray Computed Tomography. Results show that permeability evolution is strongly dependent on fluid chemistry. Undersaturated alkaline fluids dissolve the most abundant mineral phases in granite (quartz and feldspars), creating cavities along the main fractures and generating pressure-independent permeability in the core. Conversely, supersaturated alkaline fluids, resulting from extended periods of fluid-rock interactions, promote the precipitation of clay minerals, and decrease the permeability of the system. These results suggest that chemical dissolution during geothermal operations could generate permeable pathways that are less sensitive to effective stress and will remain open at higher pressures. Similarly, maintaining the circulation of undersaturated fluids through these granitic reservoirs can prevent the precipitation of pore-clogging mineral phases and preserve reservoir permeability in granite-hosted geothermal systems.

© 2020 The Authors. Published by Elsevier B.V. This is an open access article under the CC BY-NC-ND license (http://creativecommons.org/licenses/by-nc-nd/4.0/).

1. Introduction

The increasing energy demand of a growing global population combined with the urgency to reduce atmospheric CO_2 concentrations urgently call for increasing the use of geothermal systems as a low carbon alternative to other energy resources (Owusu and Asumadu-Sarkodie, 2016). Geothermal energy is one of the emerging solutions with the potential to provide renewable and sustainable energy for the future. However, as a developing sector, the geothermal industry faces many challenges to make this energy cost-effective and to achieve optimised exploitation. This study aims to address the challenge of sustaining reservoir permeability at depth by experimentally exploring the evolution of permeability in response to fluid chemistry.

Studies of the permeability evolution of the subsurface are critical to understand both natural and anthropogenic systems. In natural settings, permeability evolution is a determinant factor of fluid pressure in fault zones, which directly affects the state of stress of active faults and, thus, the onset of earthquakes (Hickman et al., 1995). For economic resources, understanding cyclic fluid-pressure fluctuations along high-angle reverse faults is critical for the exploration of valuable ore deposits, such as gold-quartz

* Corresponding author.
E-mail address: c.sanchez-roa@ucl.ac.uk (C. Sanchez-Roa).

https://doi.org/10.1016/j.epsl.2020.116641
0012-821X/© 2020 The Authors. Published by Elsevier B.V. This is an open access article under the CC BY-NC-ND license (http://creativecommons.org/licenses/by-nc-nd/4.0/).

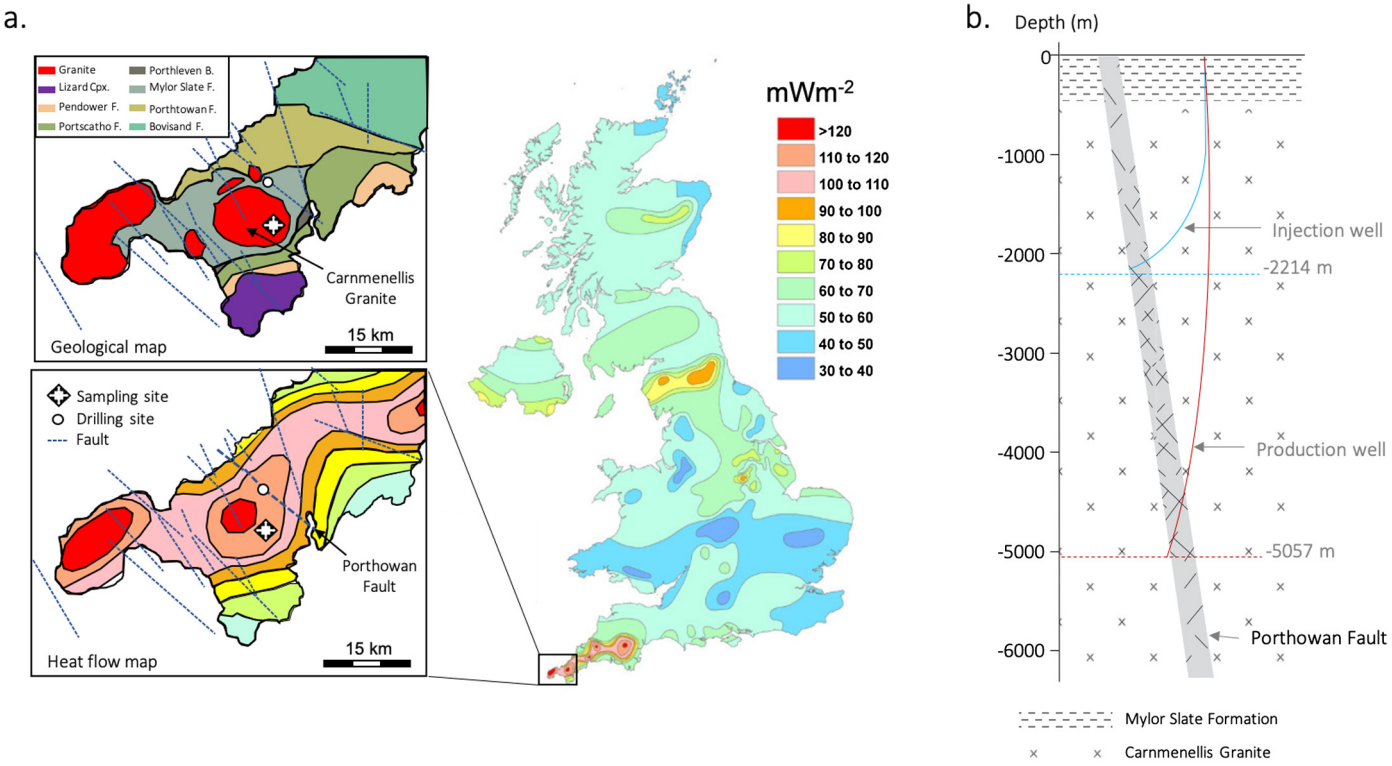


Fig. 1. a. Heat flow map of the UK, modified from the British Geological Survey (Barker et al., 2000; Busby, 2010; Lee et al., 1987; Richardson and Ronald Oxburgh, 1978; Rollin, 1995). Left: Enlargement of Cornwall, where the geological formations dictate the heat flow in the area. Sampling site indicates the location within the Carnmenellis granite where rock samples were collected. Faults plotted after *Camborne School of Mines report, 1988*. b. Drilling prospect of the UDDGP, including the injection and production wells which connect through the pre-existing fracture network of the Porthtowan fault zone. (For interpretation of the colours in the figure(s), the reader is referred to the web version of this article.)

vein systems (Sibson et al., 1988). In a similar manner, anthropogenic systems are highly dependent on permeability evolution. First, from the perspective of risk of induced seismicity, where changes in permeability can perturb the state of stress and drive faults into failure conditions during subsurface operations (Townend and Zoback, 2000). And secondly, permeability evolution is a key control on the viability and lifetime of geothermal projects (Aqui and Zarrouk, 2011). The environmental importance of maintaining permeability in geothermal reservoirs is revealed by life cycle assessments, which show that increasing the lifetime of a deep geothermal operation can significantly reduce most of the environmental impacts, including CO_2 emission per unit of electricity produced (Paulillo et al., 2020).

Fluid-rock interaction is a major contributor to permeability changes in the crust, a process that induces mineral reactions when fluids and rocks are in chemical disequilibrium (Goddard and Evans, 1995). Fluid-rock interactions along fracture systems are controlled by temperature, stress, flow rate and the chemistry of rocks and fluids. The mutual feedbacks between these factors lead to the dissolution and precipitation of minerals along the flow paths and, as a direct consequence, modify the permeability of the system (Faoro et al., 2016; Griffiths et al., 2016; Moore et al., 1994).

Physico-chemical rock properties, such as reactivity and permeability, are controlled mainly by the intrinsic properties of the reservoir rock, namely composition, texture, grain size, microfractures etc. (Oelkers et al., 2008). Granitic rocks are increasingly becoming reservoirs for geothermal projects. Their major mineral components are quartz and alumino-silicates (K-feldspar, plagioclase, micas, etc.), all of which show similar dissolution trends and dependence on pH. Quartz dissolution rates significantly increase with pH and temperature in alkaline solutions (Crundwell, 2017), whereas feldspars exhibit the slowest dissolution rates at near to neutral pH and increasing rates at both acidic and basic pH (e.g., Knauss and Wolery, 1986; Hellmann, 1994). The reactions involved in the interaction of granite with acidic fluids have been previously explored (Portier and Vuataz, 2010). However, considering the pH dependence of dissolution of granite minerals, the exploration of granite interaction with alkaline fluids is also of great importance for understanding the evolution of permeability in geothermal systems hosted in granitic rocks.

Due to its thermal potential (Fig. 1a), and the ongoing drilling of the United Downs Deep Geothermal (UDDGP) project (Ledingham et al., 2019), rocks from the Carnmenellis intrusion in Cornwall have been selected as a suitable material for this experimental study. The geology of the Carnmenellis granite has been widely studied and details on its emplacement and structural evolution can be found in (Shail and Wilkinson, 1994) and references therein. The current UDDGP targets the Porthtowan fault zone, a permeable geological structure in the Carnmenellis granite which lies approximately 800 m to the west of the United Downs drill site. Two deep wells have been drilled into the fault zone: one for injection 2214 m deep and one for production 5057 m deep (Fig. 1b). The temperature at the bottom of the production well is 195 °C, which is to date the deepest and hottest onshore well and the only planned geothermal project in deep granitic rocks in the UK.

Here we present a broad study of the processes that take place during fluid-rock interaction in granite and their effect on permeability. We report the evolution of permeability within core samples of granite after they reacted with undersaturated or supersaturated fluids (of pH ranging from 9.5 to 10.5) for five to seven days. We characterise the physico-chemical changes within the reacted cores, describe their distribution in the rock volume and discuss the role of chemical and mechanical processes that

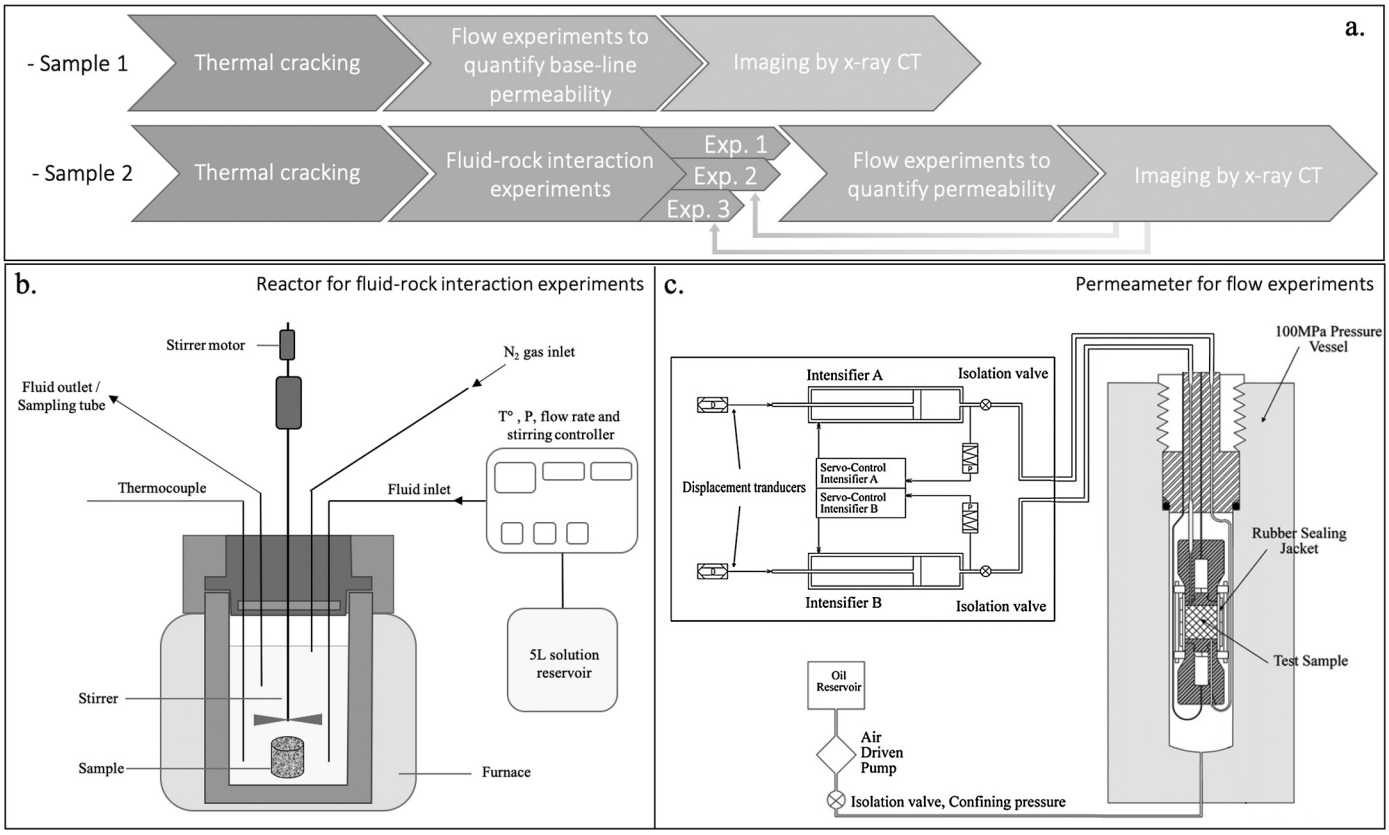


Fig. 2. a. Experimental and analytical workflow used in this study. Sample 1 is used for measuring baseline permeability and to control the extent of mechanical fracturing induced by thermal cracking. Meanwhile, sample 2 is used to perform three fluid-rock interaction experiments, each of them followed by a flow experiment to measure permeability changes and by x-ray CT imaging before starting the next experiment on this same sample in a loop approach. b. Schematic diagram of the Parr^{TM} reactor used in this study. The fluid outlet consisted of a dip-tube that was used also for sampling fluids during the batch experiment via a high-P titanium valve that kept the system closed during the experiment. The reactor is fitted with a N_2 gas inlet line to maintain pressure and an external furnace to maintain the temperature in the vessel at 180 °C. c. Schematic diagram of the permeameter system equipped with a pressure vessel filled with silicon oil as confining medium and an isolated pore pressure system with upstream and downstream servo-controlled pore fluid pressure intensifiers. During measurements the intensifiers are kept at a pressure differential that provides a precisely measured flow through the sample. The measured steady flow is used for permeability measurements when applying the steady state flow methodology (Benson et al., 2006, 2005).

control the observed changes in permeability. This combination of state-of-the-art techniques allows us to demonstrate the sensitivity of dynamic permeability to subtle changes in fluid chemistry. We use the drilling plan proposed by the UDDGP project to contextualise our results in a natural setting such as the Porthowan fault, as well as in an anthropogenic scenario using one of the most promising granitic reservoirs for geothermal energy in the UK. These results are relevant for enhancing and maintaining permeability at depth and, thus for extending the lifetime of deep geothermal projects.

2. Materials and methods

2.1. Experimental procedure

A block of medium-grained porphyritic Carnmenellis granite (50x40x20 cm) was collected from a homogeneous outcrop in Trenoweth Quarry, located 2 km SW of Penryn, Cornwall (Fig. 1). We took a single core from the collected block, which we subsequently cut into two sub-samples in order to minimise variability. Our precision coring machine enabled production of smooth cylinders of 20 mm diameter which were subsequently ground flat and parallel to achieve a set length of 20 mm ± 0.5 mm and a parallelism of better than ±0.1 mm.

The two cores were thermally treated under identical conditions to create a mechanically-induced fracture network that allows fluid flow through the samples. The thermal treatment comprised three stages: 1. heating at a rate of 10 °C/min from room temperature to a maximum temperature of 750 °C; 2. a hold period where the samples were held at the maximum temperature for 60 minutes; and 3. cooling, where the sample temperature was decreased at a rate of 30 °C/min. During the thermal cycles, a fracture network is developed due to differential thermal expansion of mineral phases during heating (Meredith et al., 2001), and the growth of tensile microcracks during cooling and contraction (Browning et al., 2016).

The first core (sample 1) was used to measure permeability curve 0, and the effect of effective pressure on the permeability of the cores without fluid-rock interaction in order to provide baseline values for comparison with the second core (sample 2) that was subject to different forms of chemical reaction in experiments 1, 2 and 3 (Fig. 2a). This procedure also measures the permeability increase after the thermal treatment in the first core, while preserving the fracture network in the second core unaltered by the pressure imposed during permeability measurements. By performing fluid interaction experiments on one single core we ensure the accuracy of computerised tomography observations and reduce the effects of natural variability in the monitoring of dissolution and precipitation of mineral phases.

The second core (sample 2) was used in the fluid-rock interaction experiments. Experiments were conducted in a Parr^{TM} titanium reactor of 300 mL internal volume (Fig. 2b). The vessel was fitted with a N_2 gas inlet line to pressurise the fluid inside

the reactor and a dip-tube for sampling fluids in batch mode. For flow-through experiments, the reacting fluid was injected into the system using a HPLC pump, while a back-pressure regulator maintained the pressure at a constant value throughout each experiment. Fluids were sampled daily to measure pH and monitor changes in concentration of the major elements present in the system (including Si, Ca, Al, K, Fe and Mg). Experimental conditions were set at a constant temperature of 180 °C and a pressure of 40 bar for all experiments. The selected temperature simulates the temperature at an approximate depth of 4.7 km, following a geothermal gradient of 38 °C/km, which is close to the temperatures found at the bottom of wells RH11, RH12 and RH15 during the Hot Dry Project (Richards et al., 1992) as well as with the temperature of well UD-1 from the UDDGP (195 °C at 5.1 km depth). The experimental pressure was set at 40 bar, which allowed for a periodic sampling of the fluid chemistry at a total pressure slightly below 40 bar.

The core was placed in the pressure vessel together with the prepared reactive fluid (see specific concentrations in supplementary information Table S1), pressurised using nitrogen gas to a final pressure of 40 bar and heated by an external heater to 180 °C. We conducted three fluid-rock interaction experiments on the same core (Sample 2, diameter: 19.7 mm, length: 20.1 mm), under the following rationale:

Experiment 1 – Undersaturated reactive fluids – Batch reactor: The core was placed into a batch reactor in contact with a reactive aqueous fluid of pH 10.5. The fluid in the reactor was continuously stirred for 6 days to measure the extent of the dissolution reactions. This experimental approach is intended to replicate natural conditions where fluids present relatively long residence times without achieving equilibrium.

Experiment 2 – Undersaturated solution – Flow-through reactor: The core was then reacted with a pH 10.6 aqueous fluid. The fluid was maintained at far from equilibrium conditions by continuous flow through system avoiding the formation of secondary phases. The flow rate was kept at 1 g/min over the first four days of the experiment and increased to 2 g/min for the last two days. This experiment was designed to simulate conditions of fluid circulation within a fractured system. Note that the twin core with the same dimensions, used for baseline permeability measurements after thermal treatment, was introduced in the reactor during this experiment as a way to verify, compare and control the reproducibility of permeability changes during the fluid-rock interaction stage.

Experiment 3 – Supersaturated reactive fluid – Flow-through reactor: The granite core was reacted in mixed-flow mode using a constant flow rate of 0.6 mL/min throughout the experiment. The aqueous solution of initial pH 9.4 was supersaturated with respect to selected secondary Mg-, Al- and Fe-rich phyllosilicate phases (see inlet fluid concentrations in Table S2). This experiment was designed to simulate a prolonged interaction between the rock and the circulating fluid. As such, fluid composition was chosen based on results of previous flow-through experiments on powdered samples and PHREEQC predictions of expected mineral phases calculated from ions released into the aqueous solution after substantial granite-water interaction.

After each experiment, the core was removed from the reactor and placed in a hydrostatic permeameter (Fig. 2c) to quantify post-reaction changes in permeability up to a maximum effective pressure of 50 MPa. This maximum pressure represents the mean stress of the Carnmenellis granite, estimated from the state of stress measured at a depth of 3.5 km (Pine and Batchelor, 1984), where: $\sigma_1 = 78.7$ MPa, $\sigma_2 = 56.7$ MPa, $\sigma_3 = 13.7$ MPa. The core was then removed from the permeameter and scanned using X-ray CT before the start of the next experiment.

2.2. Analytical methods

Textural and chemical observations of granite cores were carried out using a ZEISS EVO MA10 scanning electron microscope (SEM) at UCL. Post-reaction observations were mainly confined to the flat top surfaces of the cores. The surfaces were gold coated and analysed using back scattered electrons in atomic number contrast mode.

Fluid samples were regularly collected from the reactor during the experiments. These samples were filtered upon withdrawal from the reactors via a Ti-frit, with a nominal pore size of 5 µm, installed at the bottom of the dip-tube. Part of each sample was used to measure pH at room temperature using a traditional glass combination-electrode previously calibrated against NIST-certified buffers at pH 4.00, 7.00 and 9.21 (at 25 °C) and connected to a Mettler Toledo pH-meter. The other part of the fluid sample was acidified with ultra-high-purity HNO_3 and then stored at 3 °C until further analyses. The major element concentrations of these acidified samples were determined by inductively coupled plasma optical emission spectroscopy (ICP-OES) using a Varian 720 ES spectrometer, with detection limits varying from a minimum of 2 µg/l for Mg and Al to a maximum 12 µg/l for Si. The uncertainty of the analyses was generally lower than 2%.

2.3. Permeability measurements

Water permeability measurements were conducted using the servo-controlled hydrostatic permeameter (Fig. 2b) in the Rock and Ice Physics Laboratory at UCL, using the steady state flow methodology (Benson et al., 2005; Mitchell and Faulkner, 2008). Samples were rubber-jacketed and placed between porous alumina spacers that aid fluid distribution across the sample. The sample assembly was then inserted in the pressure vessel and sealed. The upstream and downstream servo-controlled pore fluid pressure intensifiers were set to pore pressures of 4.0 and 4.5 MPa, respectively, to provide a mean pore fluid pressure of 4.25 MPa, while maintaining a pressure difference across the sample of 0.5 MPa. Once steady state flow was achieved, consecutive permeability measurements were made over the confining pressure range from 14 to 54 MPa in 10 MPa steps, corresponding to effective pressures (P_{eff} = confining pressure – pore pressure) from 10 to 50 MPa. Permeability values were calculated using Darcy's Law using the known sample dimensions, the viscosity of water at the measurement temperature, the pore pressure gradient, and the measured steady state flow rate.

2.4. X-ray computed tomography (CT)

The three-dimensional fracture network of the granite core and any changes induced by the fluid-core interaction were imaged using a Nikon XTH225 X-Ray CT scanner. In total, 3185 projections were acquired, at 140 keV and 65 µA and a rate of 1 second per projection. The raw transmission images were reconstructed using the Nikon CT Pro 3D software package and the volume was visualised and segmented using the Avizo software (Thermo Fisher Scientific, USA).

The resulting scans had a resolution of 12 µm per pixel and the average aperture of the fractures in the core was between 50 and 60 µm. We estimate a spatial resolution of approximately 40 µm, since at least three grouped pixels are necessary for visualisation. A spatial resolution of 40 µm is close to the fracture aperture, therefore we did not perform a digital volume correlation of the entire dataset. As an alternative strategy, based on the extent of the changes in the core, we focused our analysis on changes on the outer rim of the core. Three datasets were registered manually, and top and bottom parts of the dataset were digitally removed

a.

Mineral	(Rietveld) wt %	(Normative) wt %
Quartz	32.8 ± 0.3	36.6
Albite	25.5 ± 0.3	22.8
Orthoclase	21.9 ± 0.3	19.9
Muscovite	10.9 ± 0.2	14.4
Biotite	4.2 ± 0.2	5.3
Smectite	2.6 ± 0.5	NE
Chlorite	1.6 ± 0.1	NE
Ilmenite	0.1 ± 0.1	0.2

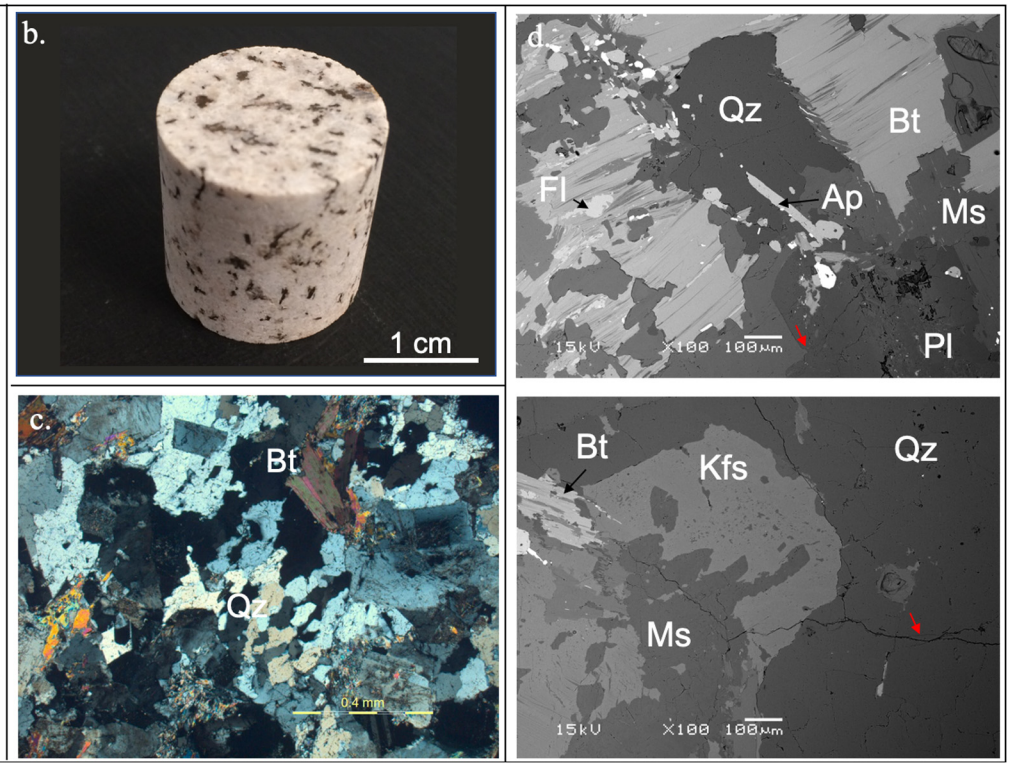


Fig. 3. a. Table of mineral composition of the Carnmenellis granite used in this study by Rietveld refinement and calculated normative composition from bulk chemical analysis. XRD data were obtained from randomly oriented powders. NE = Not examined. b. Cored sample. c. Optical microscope images of the intact sample. d. SEM observations on intact samples of the Carnmenellis granite. Microfractures are indicated with red arrows. Abbreviations: Qz = quartz, Fl = fluorite, Bt = biotite, Mu = muscovite, Pl = Plagioclase, Ap = apatite, Kfs = K-feldspar.

to avoid cone beam artefacts. Internal porosity was segmented in each dataset and the resulting volume was subtracted from the remaining datasets to quantify volume changes in the core after each experiment.

2.5. Thermodynamic calculations

Calculations of aqueous solution speciation and the saturation state with respect to relevant secondary phases were performed with the geochemical code PHREEQC v.3.5 (Parkhurst and Appelo, 2013) using the llnl database. The activity of the dissolved species was computed with extended Debye-Hückel equation. The saturation state of the aqueous fluid relative to the mineral phases of interest is expressed by the saturation index, defined as the base-10 logarithm of the ratio between the ion activity product (IAP) of the species appearing in the dissolution reaction of the mineral and the solubility product of the mineral (K_{sp}): SI = log (IAP/K_{sp}).

3. Results

3.1. Mineral characterisation of non-reacted samples

In hand specimen, the composition of the homogeneous block of fine grained Carnmenelis granite is uniform, containing phenocrystals of K-feldspar, quartz, sodic plagioclase, biotite and muscovite (Fig. 3b). Individual grain sizes range from ≈3 mm to ≈100 µm. Optical microscopy and SEM observations show accessory minerals including fluorite generally precipitated on a biotite substrate, and apatite. SEM observations show the overall integrity of the granite and lack of dissolution features in any of the mineral phases in the untreated samples. Fractures are scarce, however unconnected microfractures run through grain boundaries and tend to be slightly more abundant on quartz (Fig. 3d). The mineralogical composition in weight percent was calculated from bulk chemical analysis (normative) and by refinement of X-ray diffraction (XRD) data (of material from the same block where samples were cored) through the Rietveld method (Fig. 3-Table a).

3.2. Aqueous chemical evolution during hydrothermal alteration

The evolution of K, Si, Al, and Ca concentrations in the fluids interacting with the core as a function of time are shown in Fig. 4. The results for each experiment are described below:

Experiment 1 – Undersaturated reactive fluid – Batch reactor: The evolution of aqueous solution composition was controlled by the dissolution of quartz and feldspars, showing a progressive increase in Si concentrations, which evolved from an initial value of 0 on day 1 to 2.37 mmol/kg on day 7. Corresponding aqueous aluminium concentrations increased from 0 to 0.44 mmol/kg; and aqueous potassium concentrations increased from 0 to 0.17 mmol/kg. Ca concentration remains at low and constant value.

Experiment 2 – Undersaturated reactive fluid – Flow-through configuration: Aqueous cation concentrations during this experiment increased significantly during the first day, with aqueous Al, Ca and K concentrations attaining near constant values until day 4, after which their concentrations decreased as a consequence of the flow rate increase. Si concentration in this experiment follows a similar trend to other major cations. Note that the chemical evolution of the fluid is not cumulative since the flow-through configuration provides data of a continuously replenished fluid.

Experiment 3 – Supersaturated reactive fluid – Flow-through configuration: Most significant changes in the aqueous cation concentrations occurred during the first two days of this experiment. This is evidenced by the sudden decrease in the concentrations of aqueous Mg, Ca, and Al, suggesting the precipitation of secondary phases. Potassium concentration increases over the same time interval, whereas Si shows a slight concentration increase only dur-

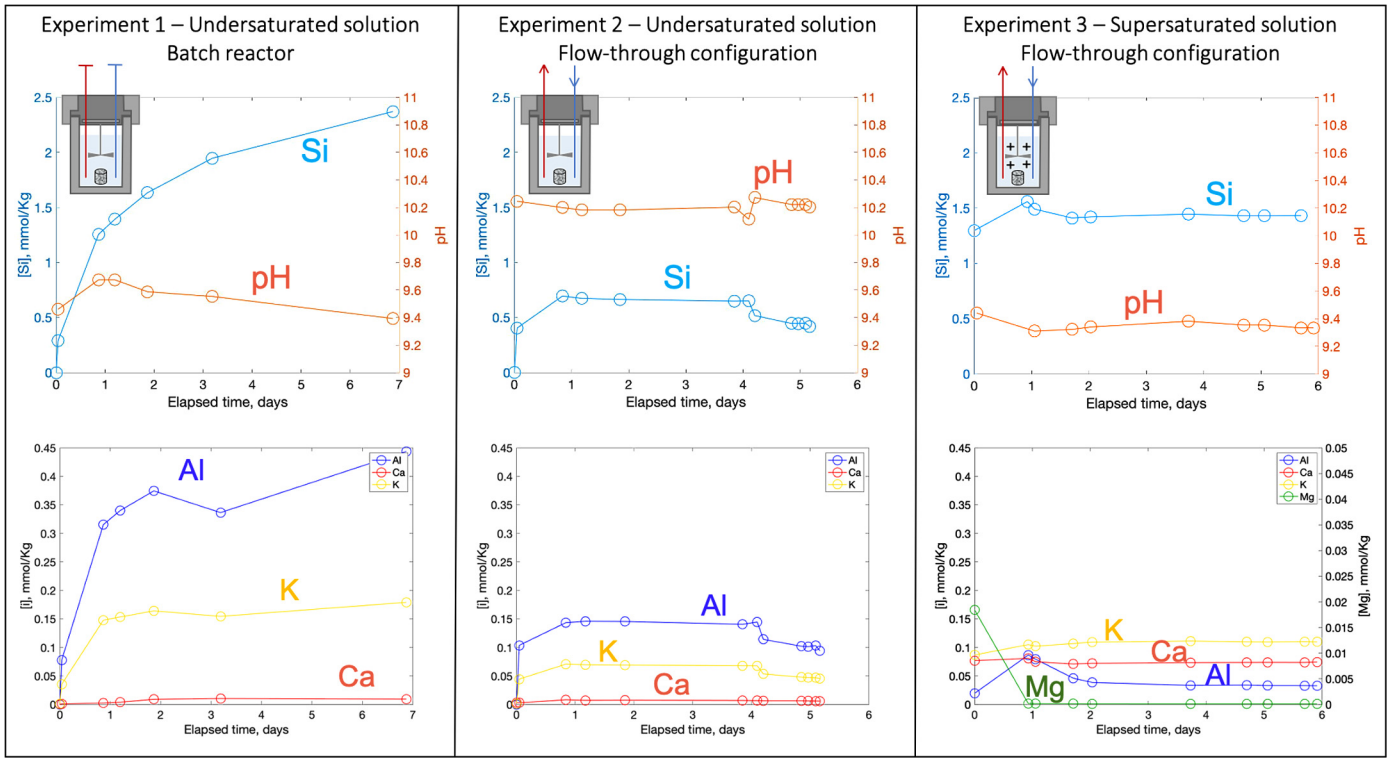


Fig. 4. Temporal chemical evolution of pH and major cations in the fluids of the three experiments performed sequentially on a single granite core. Error on the elemental analyses is estimated to be <2% and is represented within the size of the symbols on the plot. For each experiment, pressure and temperature were kept constant at 4 MPa and 180 °C. Experiments 1 and 2 started with an undersaturated solution (distilled water), while experiment 3 started with a supersaturated solution (with respect to clay minerals).

ing day 1, and continues to be released to the solution at a steady rate over the rest of the experiment. Except for Ca and Mg, the concentrations of the remaining elements exhibit a net increase compared to the inlet fluid, indicating the ongoing dissolution of primary phases.

3.3. Permeability evolution due to chemical alteration

The permeability of the intact granite cores (before thermal treatment) was 2.30×10^{-21} m^2 at an effective pressure of 10 MPa. Steady state flow was achieved in around three days, which is considered slow and indicative of low sample permeability. Measurements were therefore not performed at higher effective pressures. Thermal treatment of the cores resulted in a network of cracks that increased the permeability of the granite by approximately five orders of magnitude (see the resulting fracture network in supplementary information Video 1).

The permeability evolution of the cores after fluid-rock interaction experiments is shown in Fig. 5, with the permeability of the thermally-treated but unreacted core also included for comparison.

The permeability of the thermally cracked but unreacted core (black line in Fig. 5) is strongly dependent on effective pressure. The permeability of the core is 1.52×10^{-16} m^2 at 5 MPa effective pressure. This permeability decreases to 1.22×10^{-16} m^2 as the effective pressure is increased to 50 MPa. Following this, the effective pressure is reversed and gradually decreased following the same pressure steps. However, while the permeability increases during this pressure decrease, it does not fully recover its initial, pre-pressurisation value. The crack closure that occurs as effective pressure is increased, involves both elastic and inelastic processes, but only the elastic part is recovered during the pressure decrease. This results in the observed permeability deficit, which is a manifestation of hysteresis. Note that permeability hysteresis is observed in all experiments, with the initial permeability, measured at low effective pressure, never being fully recovered after the effective pressure is increased to 50 MPa and then lowered back to its initial value. This resulted in a permeability deficit of 6.21×10^{-17} m^2 measured on the unreacted core at 10 MPa after pressurisation and de-pressurisation.

After reaction with an undersaturated solution in a closed system reactor (experiment 1), the permeability of the core shows a strong dependence on effective pressure up to 30 MPa, but a much weaker dependence at higher pressures (red line in Fig. 5), remaining around 3-8 $\times 10^{-18}$ m^2 for confining pressures increasing from 30 to 50 MPa. The permeability decreased from 1.8×10^{-16} m^2 at 5 MPa effective pressure to 4.01×10^{-18} m^2 at 50 MPa. Again, hysteresis is observed with a permeability deficit of 7.62×10^{-17} m^2 at 10 MPa.

After interacting with an undersaturated solution in the flow-through system (experiment 2, green line on Fig. 5) the permeability of the core is significantly higher. The permeability was 4.92×10^{-16} m^2 at 5 MPa effective pressure and decreased to 2.78×10^{-17} m^2 at 50 MPa. We observe a similar pressure dependence to that seen after experiment 1, but more hysteresis and a larger permeability deficit of 2.51×10^{-16} m^2 at 10 MPa.

After reaction with a supersaturated fluid in the flow-through system (experiment 3, blue line on Fig. 5) the reacted core exhibits lower permeability, which decreased by approximately an order of magnitude since experiment 2. The permeability after experiment 3 was 1.25×10^{-17} m^2 at 5 MPa effective pressure and decreased to 5.62×10^{-18} m^2 at 50 MPa. Again, the pressure sensitivity of the permeability decreases with increasing effective pressure. However, the reacted core recovered from this experiment exhibits the least hysteresis and the lowest measured permeability deficit of 6.75×10^{-18} m^2 at 10 MPa.

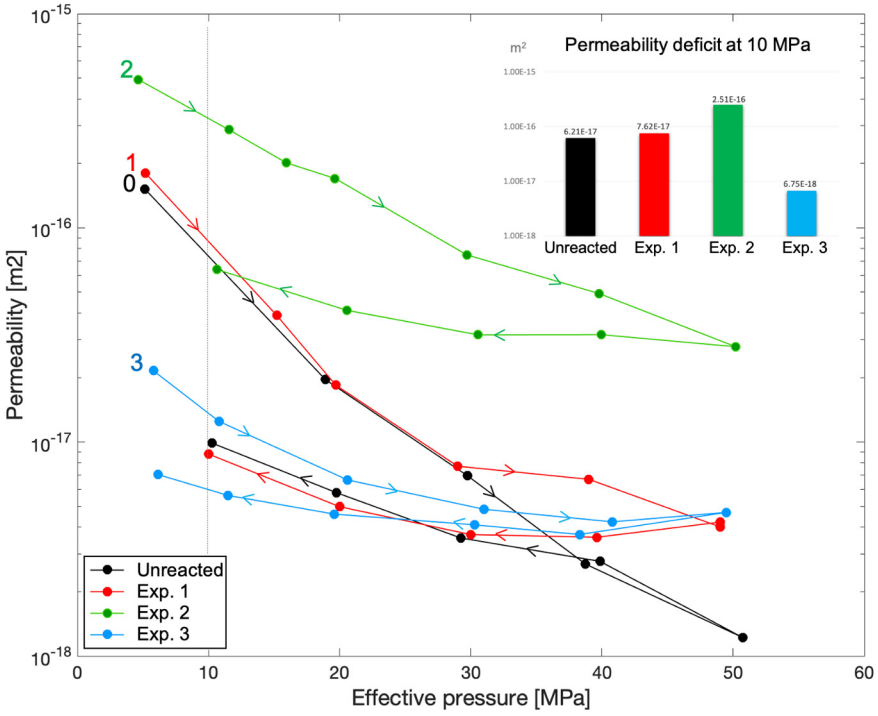


Fig. 5. Permeability evolution as a function of effective pressure for a thermally cracked Carnmenellis granite core before and after three fluid-rock interaction experiments. The black curve shows the permeability measured in the unreacted core; the red, green, and blue curves correspond to the permeability measured after it was recovered experiments 1, 2, and 3, respectively. The high accuracy by which the hydraulic pumps control the pressure difference across the sample and measure the flow rate led to minimal errors in the measurements, which are smaller than the size of the symbols in the graph. Inset: Deficit between the initially measured permeability at 10 MPa (grey dotted line) and that measured at the same pressure after the full pressurisation/depressurisation cycle.

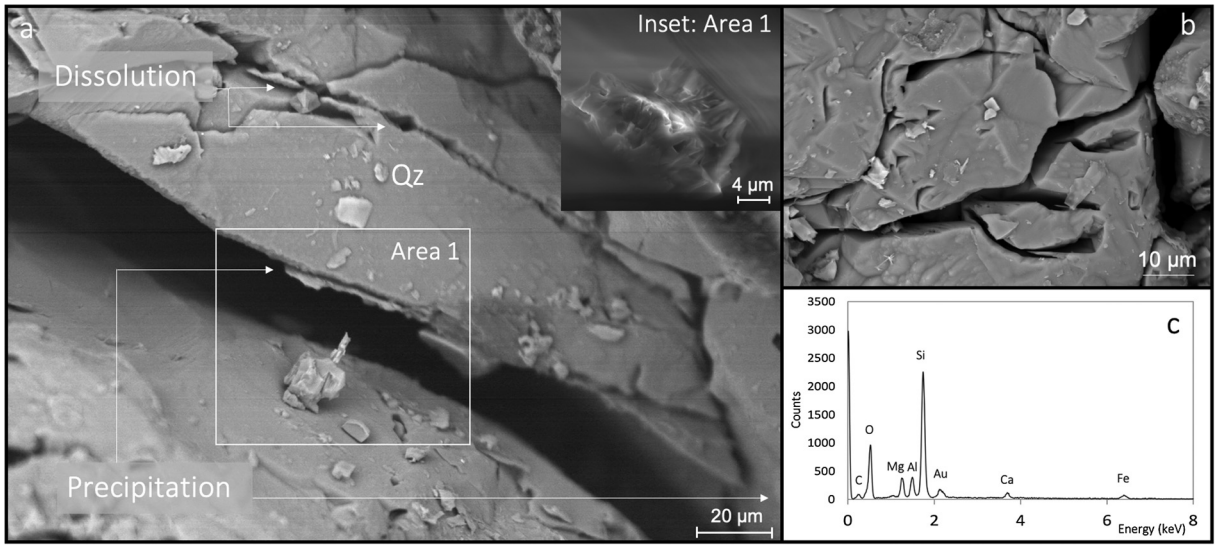


Fig. 6. a. Backscattered electron image showing the ground top surface of the reacted core after experiment 3, illustrating dissolution along fractures and mineral precipitation on fracture walls. Inset: secondary electron image of the interior of the fracture seen in (a) showing a mineral precipitate. b. Backscattered electron image showing the angular dissolution etch pits in a quartz grain. c. Energy-dispersive X-ray analyses of the precipitated material in area 1, showing the elemental composition of the precipitate, which is qualitatively similar to an aluminium silicate containing Mg, Fe and Ca.

3.4. Microstructural observations of reacted samples

SEM observations on the gold-coated ground top surface of the core recovered from experiment 3 (Fig. 6) show the presence of connected microfractures. Some of these microfractures show evidence of dissolution (Fig. 6a), including the development of etch pits in proximity to the fracture openings and the rounded morphologies of their edges, whereas others show mineral precipitates attached to the fracture walls. EDS analysis of one of these precipitates is shown in Fig. 6c. The foliated morphology together with the EDS spectrum suggest it consists of an aluminium silicate containing Mg, Fe and Ca, possibly a phyllosilicate of the smectite group.

3.5. X-ray computed tomography imaging of reacted samples

CT results of the core recovered after experiments 1 to 3 are presented in Fig. 7, and show that core volume loss is concentrated at the outer core surface. The analysed surface shows quantifiable volume loss during experiment 2, constituting a solid volume loss

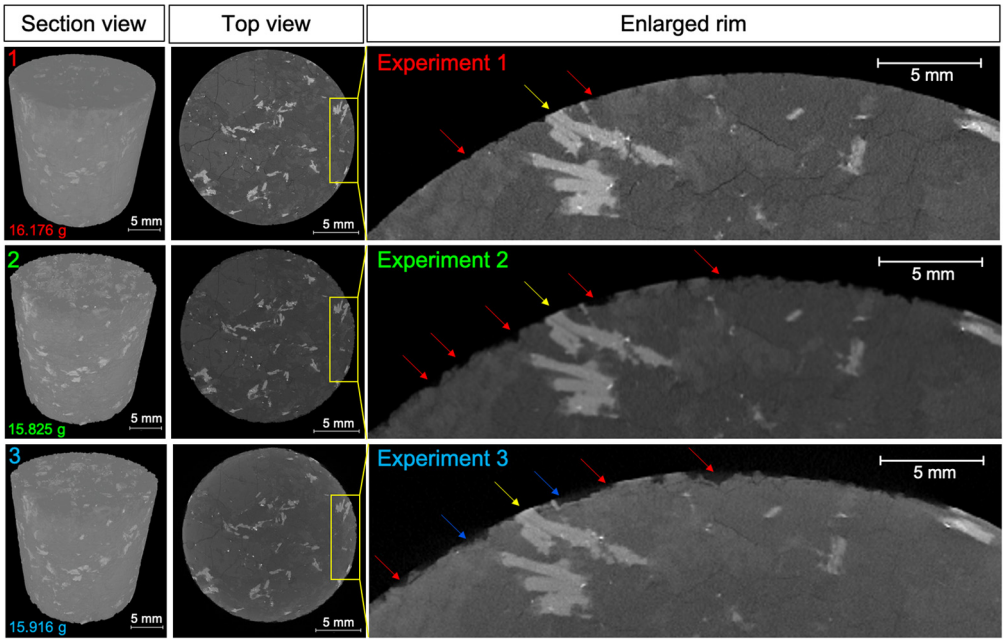


Fig. 7. Computed tomography images of the core recovered after experiments 1, 2 and 3. Column 1 shows the rendered volumes after stacking with the software Avizo. Column two shows the corresponding top view. Column 3 shows an enlargement of the morphological changes on a magnified area along the core edge. The density contrast between the minerals present is reflected in three main grey tones of the image: quartz and plagioclase appear in dark grey, micas in bright light grey and K-feldspar in medium grey. Red arrows point to material lost. Blue arrows point to material gained. Yellow arrows point to areas that show no evidence of dissolution mostly related to high density minerals (micas).

of around 1.55%, which is equivalent to a total of ~95 mm^3 of removed material (Fig. 8). By the end of experiment 3 there is a less significant but notable increase in solid volume, amounting to approximately 30 mm^3 of added material, or 0.49% extra solid volume in the core. However, when subtracting the segmented volume of experiment 3 from 2, there is also a negative difference in the overlapped volumes, where areas that were previously solid appear to have become voids. This indicates that around 10 mm^3 of material was removed during this stage (~0.17%), so that the net increase of volume that took place during experiment 3 corresponds to ~20 mm^3 of solids (~0.32% of the total volume) (Fig. 8).

4. Discussion

4.1. Mineral dissolution in granite and volume loss at alkaline pH

The chemical compositions of the reactive fluids after experiments 1 and 2 are dominated by Si, Al, K, Na and Ca (Fig. 4). These elements are released from the granite and suggest the dissolution of quartz, plagioclase and K-feldspar, which together constitute ~80% of the rock mass (Table 1). This is consistent with data and derived rate equations reported by Palandri and Kharaka (2004), and with in-situ flow experiments in Cornwall (Richards et al., 1992). The contribution of the remaining mineral phases to the dissolution process, mostly biotite and muscovite, is negligible over the timescale of the study, likely due to their sluggish reactivity relative to the dominant minerals (Knauss and Wolery, 1989; Nagy, 1995). This is supported by the absence of distinguishable physical changes on the mica grains in the CT data (yellow arrows in Fig. 7).

As shown by the CT analysis (Fig. 8), the dissolution of the granite core after the first two experiments accounts for the loss of approximately 1.55% of the initial core volume, for a total of ~95 mm^3 removed (total dissolution volume segmented after the completion of experiment 2, Fig. 8 left column). An independent estimate of the mass of granite dissolved during these two experiments can also be obtained from mass balance calculations based on the total mass of the elements released to the fluid. In making such calculations we assumed that the measured dissolved Ca was supplied by plagioclase dissolution, from which we derived the corresponding amounts of Al, Si and K, as fixed by the mineral stoichiometry. This assumption allowed calculation of the amounts of Al, K and Si released by K-feldspar and, finally, the Si mass provided by quartz dissolution, and their corresponding mineral volumes. The results of these calculations suggest that approximately 145 mm^3 of rock were dissolved, which correspond to a mass loss of 2.36%. The difference between this estimate and the volume loss calculated from tomography data is attributed to dissolution taking place in areas of the core that were not included in the CT analysis, and indicates that approximately 50 mm^3 of volume was lost from the innermost part of the core. Approximately the same material loss is evidenced by measurement of the dry rock sample weight before and after the two dissolution-controlled experiments (Table S2) which indicates a mass decrease of 2.5%.

4.2. Dissolution geometry and permeability increase

Partial dissolution of quartz and feldspars generated secondary porosity (Fig. 6), which had a strong impact on core permeability (Fig. 5). The dissolution of quartz surfaces has previously been described as taking place at crystal edges and kinks (Brantley et al., 1986). These surface features can be preferentially exposed after mechanical fracturing, because the fractures tend to propagate along grain boundaries. The dissolution process often results in angular pitting on quartz surfaces and is largely controlled by the dissolved silica concentration in the solution (Brantley et al., 1986). In this study, dissolution on fracture surfaces around quartz grains are observed to result in surface pitting (Fig. 6a and 6c).

CT images show that external areas of the core that were in direct contact with the fluid show the largest amount of dissolution. This created an alteration halo towards the core's rim and a less altered volume towards the inner parts of the core. Changes in the fracture paths are reflected in a noticeable increase of permeability during experiment 2, from 8.78×10^{-18} m^2 (last permeability

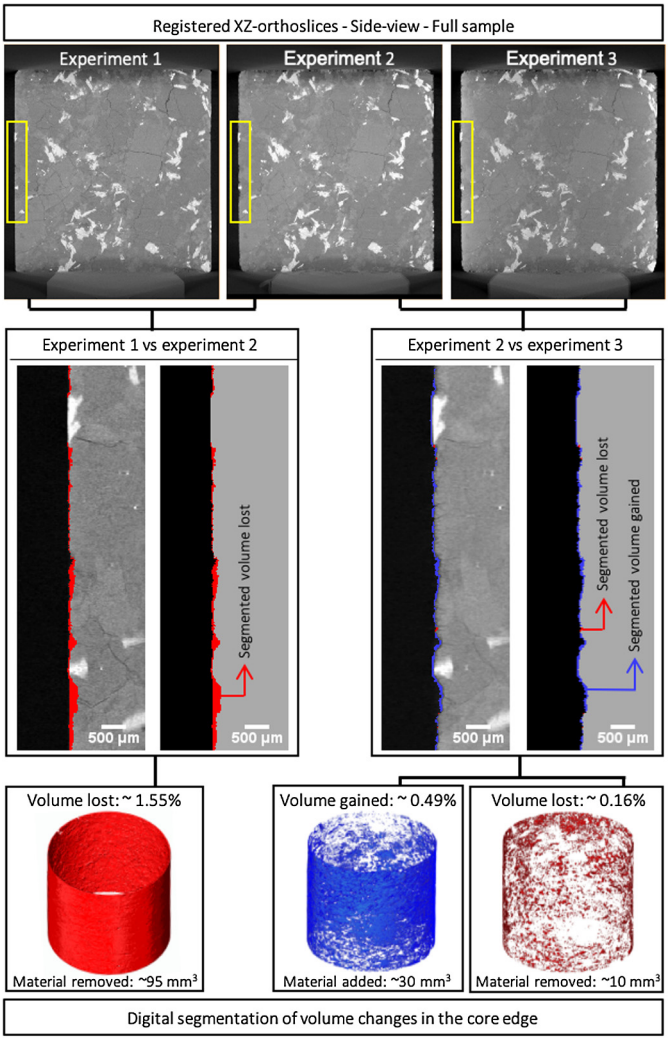


Fig. 8. Distribution of mineral volume gains and losses in the core due to the three sequential experiments performed in this study. Top row shows three 2-dimensional slices (XZ-orthoslices) of the three scan datasets, which have been digitally aligned into one coordinate system (registered), on which the segmentation of the core edge is based. Second row shows the digital segmentation of volume lost (red) or gained (blue) after comparing the core volume after experiment 1 against the volume after experiment 2 (left) and the results of the volume comparison between experiment 2 and experiment 3 (right). The bottom row shows the results of volume comparison between experiments 1 and 2 on the entire rim of the core, where only volume loss was detected (left) and the volume comparison between experiments 2 and 3 (right), where both volume gain and loss were detected.

measured on the core after experiment 1) to 2.5×10^{-16} m^2 (first permeability measured on the core after experiment 2). It is important to note that the permeability values reported in this study are calculated on the entire core's cross-sectional area, thus they constitute an average value between the permeability of the alteration halo and the less altered internal areas. This indicates that the permeability values reported in this study may constitute a lower threshold of the measured effects of the reactions regarding the permeability of the core.

The etching of pre-existing fracture surfaces during runs 1 and 2 increases their roughness, which in turn increases the permeability because rougher cracks are less easily closed by applied pressure (Pérez-Flores et al., 2017; Wang et al., 2016) (Fig. 7 and Fig. 8). Mechanically this surface roughness can be related to the permeability deficit after de-pressurisation, which is higher for experiments 1 and 2 (inset in Fig. 5). This permeability deficit can be representative of the increased number of asperities that undergo comminution during the pressure cycling (Wang et al., 2016). The new dissolution-induced porosity develops to an increasing level of connectivity as dissolution progresses. We characterise the initial fractures as mated, in the sense that opposing fracture surfaces have no shear offset and are therefore mirror images of each other. When such mated fractures are subjected to pressure, they are able to close fully, resulting in the closing off of fluid flow paths and a decrease in permeability to a value very close to that of the intact sample (Nara et al., 2011). Because of new dissolution-induced porosity, the fracture surfaces become unmated, meaning they are no longer mirror images. This means that fracture apertures remain partially open even under significant effective pressure, maintaining flow paths that considerably increase permeability (Pérez-Flores et al., 2017). Similar to our results, the increase in permeability from mated to unmated fractures reported by Pérez-Flores et al. (2017) also increases with greater effective pressure, especially for small offsets.

The larger permeability differences observed in our experiments at higher effective pressures (>30 MPa) indicate that dissolution-induced microstructural changes of the fracture surfaces allow permeable pathways to remain open after extensive fluid-rock interaction under increasing effective pressures, where unreacted fractures would be closed (Fig. 5). This may partially explain why the core permeability is relatively insensitive to pressure at pressures above 30 MPa following chemical treatment. In this way, dissolution along the fracture planes can significantly affect the rock´s physical properties by enhancing the permeability of the fracture system and maintaining its hydraulic properties under high stress regimes. This is most clearly seen when comparing the permeability measurements of the unreacted core and the core recovered after the first experiment (red and black curves in Fig. 5). Here, the two curves are essentially identical at effective pressures up to 30 MPa but diverge significantly at higher pressures. For the unreacted core with mated microfractures (black line), the permeability continues to decrease at higher pressures, indicating continued crack closure. In contrast, for the reacted core after experiment 1 (red line), the presence of even limited dissolution features allows permeable pathways to remain open at higher effective pressures, resulting in virtually no further permeability decrease. This likely results from the formation of "compound fractures" due to the dissolution process, where the initially mated fractures become etched and unmated in some parts, while some parts of the fracture surfaces remain mated. When pressure is applied to the fracture the mated parts tend to close up (and reduce permeability) but the unmated parts remain at least partially open. There is therefore a "critical pressure" at which the mated parts become closed and there is essentially no flow through these parts. An effective pressure of 30 MPa appears to mark the "critical pressure" at which the permeability due to changes in crack surface morphology induced by dissolution begins to dominate over the pre-existing cracks that close at elevated pressure. This threshold may vary with different rocks and fracture systems, because the initial roughness and the effects of dissolution will vary with mineralogy and fluid chemistry. However, we expect the underlying process to persist and scale with fracture aperture and degree of alteration.

4.3. Mineral precipitation and permeability decrease

Fluid flow in the crust, whether related to meteoric water, deep sedimentary basin brines or to metamorphic fluids, promotes fluid-rock interactions that result in chemical changes in both fluids and rocks (Goddard and Evans, 1995). The fluid composition in experiment 3 was selected to include ions released into the aqueous solution after granite-water interaction. For this reason, the inlet fluid was enriched in Si, Al, K, Ca, Mg, and Na and supersaturated with respect to some phyllosilicates. The evolution of the satura-

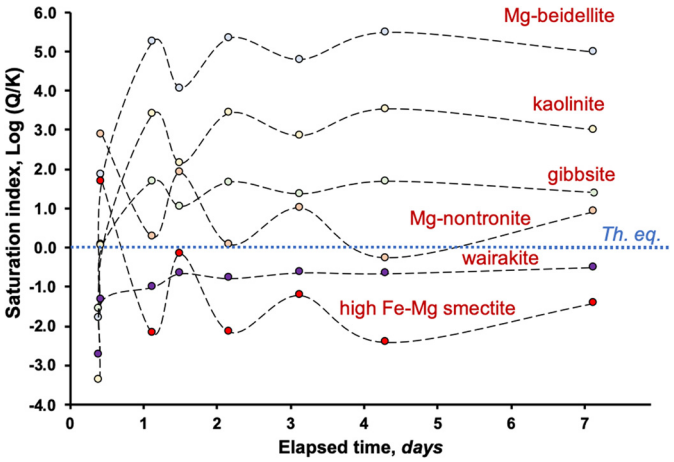


Fig. 9. Temporal evolution of the saturation indices of the reactive fluid during flow-through experiment 3 with respect to selected secondary phases, as calculated with PHREEQC using the llnl database. The blue dotted line at SI = 0.0 represents the conditions of thermodynamic equilibrium between the fluid and the solid phases.

tion indices of the reactive fluid during experiment 3 with respect to a number of relevant secondary phases is shown in Fig. 9, where phases with positive saturation indices are those prone to precipitation during the experiment.

The interaction of this supersaturated solution with the granite during experiment 3 resulted in a permeability decrease of approximately half an order of magnitude, from 6.38×10^{-17} m^2 (by the end of the permeability measurements after experiment 2) to 1.25×10^{-17} m^2 at 10 MPa effective pressure (measured on the same core after experiment 3) (Fig. 5). This permeability change suggests that new mineral phases precipitated within the fractures in the core. In addition, the hysteresis (permeability deficit) values for experiment 3 are the lowest recorded among all the experiments (inset in Fig. 5.), suggesting a decrease in the number of microcontacts that undergo comminution during the pressure cycling (cf. Wang et al., 2016), and/or the presence of more compliant materials that deform in a more plastic manner, such as, swelling clays, as it has been observed in deformation experiments and microstructural observations (Ikari et al., 2009; Lockner et al., 2011; Sánchez-Roa et al., 2018, 2017).

The chemical changes observed in the reactive aqueous fluid throughout experiment 3, specifically the decrease in Mg, Al and Si concentrations (Fig. 4c), are consistent with the precipitation of alumino-silicates such as those considered in Fig. 9. The SEM-EDS analysis of mineral precipitates observed within the core fractures (Fig. 6d) also supports the interpretation that clay minerals are the secondary product of this fluid-rock interaction. The identity of the mineral phase or phases that precipitated within the fractures could not be determined due to their very small grain size. Nevertheless, based on the measured chemical changes in the reactive fluid composition and thermodynamic calculations, it is reasonable to suggest that Mg-smectites formed during the experiments (Fig. 9). If the precipitates consisted only of Mg-nontronite ($Mg_{0.175}Al_{2.35}Si_{3.65}H_2O_{12}$), Mg-beidellite ($Mg_{0.175}Al_{2.35}Si_{3.65}O_{10}(OH)_2$) or a mixture of these two phases, then, based on the observed decrease in Mg concentration, the amount formed would produce a solid volume of approximately 400 mm^3 (an increase of ~6.7% relative to the initial core volume). However, because of the higher Mg content in the stoichiometry of Fe-Mg smectite ($Ca_{0.25}Na_{0.1}K_{0.2}Fe_{0.7}Mg_{1.15}Al_{1.25}Si_{3.5}H_2O_{12}$), the solid volume calculated assuming the precipitation of this phase would be around 60 mm^3 (~1% of the initial core volume).

The effect of secondary phase precipitation on permeability is difficult to assess, due to the concurrent dissolution of primary phases, as revealed by volume correlation analysis of CT data at the end of experiment 3 (Fig. 8), which indicates that both dissolution and precipitation reactions occurred during this experiment. Nonetheless, the overall volume gain and permeability reduction indicate that precipitation significantly impacts pore connectivity. This newly precipitated material is likely to: (1) clog fluid flow paths, thus decreasing porosity; (2) increase the tortuosity of the permeable paths; and (3) decrease the permeability of fluid pathways according to the organisation, location, and physical properties of the newly crystallised minerals (Aben et al., 2017; Heap et al., 2020). For example, the water permeability of clay minerals relevant to this system is low even at low effective pressures (< 10 MPa), as is the case of kaolinite (around 8×10^{-20} m^2) and swelling clays such as montmorillonite (as low as 9×10^{-23} m^2) (Behnsen and Faulkner, 2011).

4.4. Implications for fluid flow at depth and in the United Downs Geothermal Project

Because of the low matrix permeability of granite, engineered geothermal systems hosted in granitic rocks commonly require the generation of enhanced fracture networks, generally through hydraulic fracturing. Alternatively, wells can be drilled to target existing fractured areas, which create permeable structures within the granite body (e.g. faults or damage zones) (Wyborn et al., 2005). This study focused on the interactions between fractures in granite and moderately high pH fluids under hydrothermal conditions. Thus, the results and conclusions are applicable to natural and anthropogenic fracture networks under hydrothermal conditions.

The originally impermeable Carnmenellis granite cores were thermally cracked in order to generate a permeable fracture network, a stage that is often required in low-permeability reservoirs. The thermal treatment produces a large number of new tensile fractures that interconnect and significantly increase core permeability (supplementary information, Video 1); a result that is comparable to other mechanical fracturing techniques (Solberg et al., 1980; Watanabe et al., 2017). Considering the observations of this study, we propose the following potential evolution of permeability of granite in geothermal systems (Fig. 10). First, a mechanically fractured granitic reservoir is in contact with dilute fluids flowing through the newly created fracture network. Over time, the interaction of the rock with an undersaturated fluid leads to semi-static or continuous flow conditions (experiments 1 & 2). Due to dissolution the composition of the fluid is progressively enriched in metals released from the minerals, while the microfracture spacing increases and surfaces become rougher. After extended interactions, the fluid becomes supersaturated with a number of secondary phases, leading to precipitation (experiment 3), particularly in fractures with restricted fluid circulation, where the aqueous fluid can reach higher degrees of supersaturation.

The effective pressures at which permeability were measured in this study correspond to the range of expected effective pressures in the Carnmenellis granite at depths between 500 m and 5 km. Given the observed 30 MPa cut-off for the permeability dependence (Fig. 5), these results are particularly relevant for the UDDGP, where the effective pressures between the injecting and producing boreholes range from around 25 to 45 MPa making the permeability and therefore the productivity of the system highly dependent on effective stress. These results suggest that enhancing mineral dissolution with highly reactive fluids during geothermal operations in granites, could potentially generate new permeability that is less sensitive to effective stress and will be maintained at higher pressures. In contrast to low pH treatments, our results suggest that the use of moderately high pH solutions (pH 9 to 10.5 or higher) is an effective method for permeability enhancement in granitic systems. Additionally, the use of alkaline fluids should reduce the mobility of potentially toxic heavy metals by

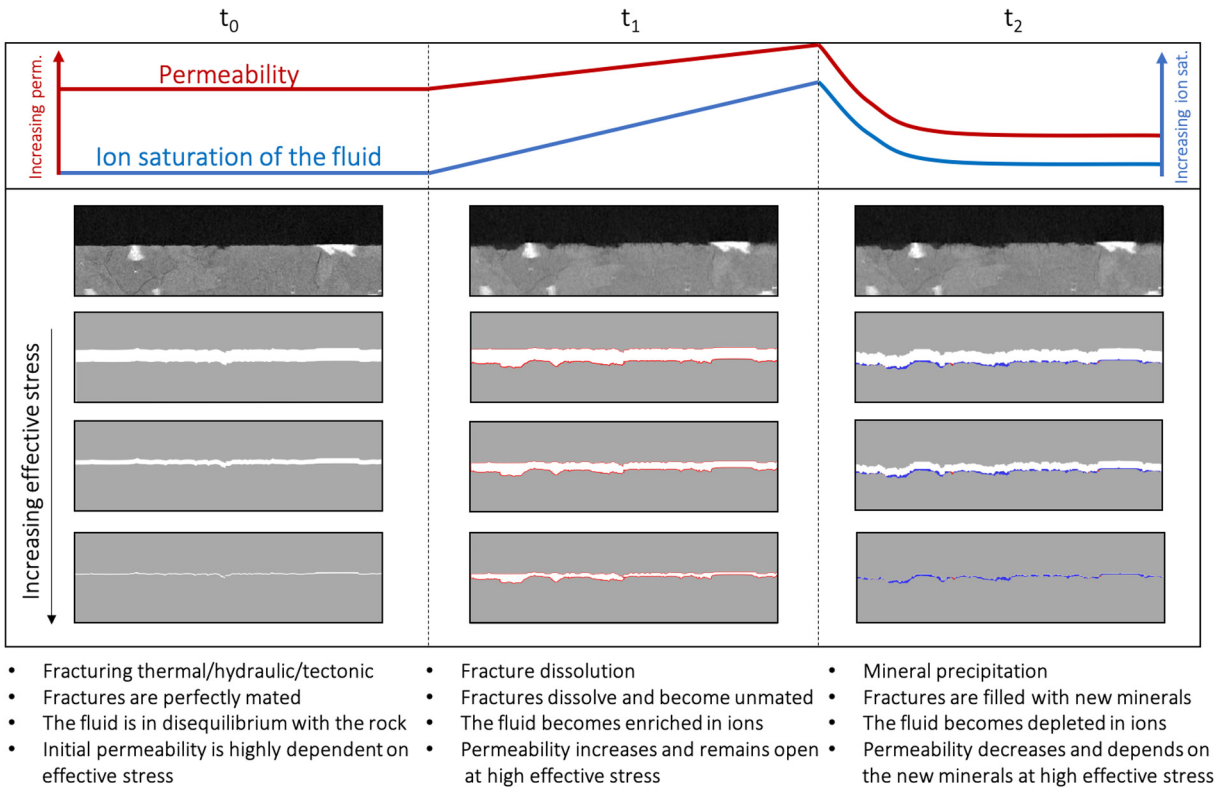


Fig. 10. Conceptual model of fluid-rock interaction within fractures in thermally cracked granites such as investigated in this study. t_0 refers to a post-fracture stage when a fracture network is originally created, and fluid-rock interaction commences. t_1 represents an intermediate stage of fluid-rock interaction with an undersaturated fluid that leads to mineral dissolution, rougher surfaces and a consequent permeability increase. During t_1 the composition of the fluid is progressively enriched in metals released from the minerals. Finally, t_2 presents a stage of extended interaction, when the supersaturated fluid reaches a precipitation stage leading to fracture sealing and a permeability decrease which largely depends on the properties of the secondary minerals precipitated.

favouring their fixation into metal oxides, such as ilmenite and Fe-oxyhydroxides, either present or forming during the circulation of the fluids in the reservoir rock (Cowan et al., 1991; Musić and Ristić, 1988).

5. Conclusions

This study shows that the permeability of granite can increase by two orders of magnitude in only five days when in contact with alkaline undersaturated solutions (pH 10-10.5) that promote dissolution within pre-existing fractures. In contrast, permeability decreases by over half an order of magnitude in six days when in contact with supersaturated solutions (pH 9-9.5) that promote the precipitation of clay minerals.

Geomechanical results show pressure dependence of the newly created permeability of reacted core up to 30 MPa, and insensitivity at pressures higher than 30 MPa. We interpret the dissolved fractures as unmated at the microscale, allowing for the fluid paths to remain open and maintain permeability at higher confining pressures. Consequently, we suggest that dissolution in the early stages of geothermal operations could help generate permeable pathways that can become crucial at maintaining permeability at depth.

Precipitation of secondary phases due to chemical evolution of the fluid can significantly alter the fluid flow geometry and permeability distribution in the host rock (Bossennec et al., 2018; Farrell et al., 2014). Understanding the reactions occurring at the microstructural scale is thus fundamental to prevent drastic reductions of the permeability of the system and extend the productivity of geothermal reservoirs.

The results of this study highlight the importance of fluid-rock interactions in geothermal systems, where the interplay between dissolution and precipitation reactions defines reservoir permeability. Permeability is a crucial parameter in the lifespans of geothermal systems (Aqui and Zarrouk, 2011), thus fluid-rock interaction can vastly affect the environmental performance of energy, since performance increases the longer heat and power generation are sustained (Paulillo et al., 2020). Therefore, efforts to find sustainable ways of keeping and enhancing reservoir permeability in geothermal systems can contribute to lowering CO_2 emissions and sourcing more sustainable energy.

CRediT authorship contribution statement

All authors discussed the results and contributed to the final manuscript.

Declaration of competing interest

The authors declare that they have no known competing financial interests or personal relationships that could have appeared to influence the work reported in this paper.

Acknowledgements

The authors acknowledge financial support from the Science4CleanEnergy consortium (S4CE), which is supported by the Horizon 2020 R&D programme of the European Commission, via grant No. 764810. We thank L. Cotton, R. Law and the GeoScience Limited team for advice on sampling sites and valuable discussions. Finally, we thank Associate Editor Dr. H. Handley and two anonymous reviewers for their insightful comments.

Appendix A. Supplementary material

Supplementary material related to this article can be found online at https://doi.org/10.1016/j.epsl.2020.116641.

References

Aben, F.M., Doan, M.L., Gratier, J.P., Renard, F., 2017. Experimental postseismic recovery of fractured rocks assisted by calcite sealing. Geophys. Res. Lett. 44, 7228–7238. https://doi.org/10.1002/2017GL073965.

Aqui, A.R., Zarrouk, S., 2011. Permeability enhancement of conventional geothermal wells. In: New Zeal. Geotherm. Work. 2011.

Barker, J.A., Downing, R.A., Gray, D.A., Findlay, J., Kellaway, G.A., Parker, R.H., Rollin, K.E., 2000. Hydrogeothermal studies in the United Kingdom. Q. J. Eng. Geol. Hydrogeol. 33, 41–58. https://doi.org/10.1144/qjegh.33.1.41.

Behnsen, J., Faulkner, D.R., 2011. Water and argon permeability of phyllosilicate powders under medium to high pressure. J. Geophys. Res., Solid Earth 116, 1–13. https://doi.org/10.1029/2011JB008600.

Benson, P., Schubnel, A., Vinciguerra, S., Trovato, C., Meredith, P., Young, R.P., 2006. Modeling the permeability evolution of microcracked rocks from elastic wave velocity inversion at elevated isostatic pressure. J. Geophys. Res., Solid Earth 111. https://doi.org/10.1029/2005JB003710.

Benson, P.M., Meredith, P.G., Platzman, E.S., White, R.E., 2005. Pore fabric shape anisotropy in porous sandstones and its relation to elastic wave velocity and permeability anisotropy under hydrostatic pressure. Int. J. Rock Mech. Min. Sci. 42, 890–899. https://doi.org/10.1016/j.ijrmms.2005.05.003.

Bossennec, C., Géraud, Y., Moretti, I., Mattioni, L., Stemmelen, D., 2018. Pore network properties of sandstones in a fault damage zone. J. Struct. Geol. 110, 24–44. https://doi.org/10.1016/j.jsg.2018.02.003.

Brantley, S.L., Crane, S.R., Crerar, D.A., Hellmann, R., Stallard, R., 1986. Dissolution at dislocation etch pits in quartz. Geochim. Cosmochim. Acta 50, 2349–2361. https://doi.org/10.1016/0016-7037(86)90087-6.

Browning, J., Meredith, P., Gudmundsson, A., 2016. Cooling-dominated cracking in thermally stressed volcanic rocks. Geophys. Res. Lett. 43, 8417–8425. https://doi.org/10.1002/2016GL070532.

Busby, J., 2010. Geothermal prospects in the United Kingdom. In: Proc. World Geotherm. Congr., pp. 25–29.

Cowan, C.E., Zachara, J.M., Resch, C.T., 1991. Cadmium adsorption on iron oxides in the presence of alkaline-Earth elements. Environ. Sci. Technol. 25, 437–446. https://doi.org/10.1021/es00015a009.

Crundwell, F.K., 2017. On the mechanism of the dissolution of quartz and silica in aqueous solutions. ACS Omega 2, 1116–1127. https://doi.org/10.1021/acsomega.7b00019.

Faoro, I., Elsworth, D., Candela, T., 2016. Evolution of the transport properties of fractures subject to thermally and mechanically activated mineral alteration and redistribution. Geofluids 16, 396–407. https://doi.org/10.1111/gfl.12157.

Farrell, N.J.C., Healy, D., Taylor, C.W., 2014. Anisotropy of permeability in faulted porous sandstones. J. Struct. Geol. 63, 50–67. https://doi.org/10.1016/j.jsg.2014.02.008.

Goddard, J.V., Evans, J.P., 1995. Chemical changes and fluid-rock interaction in faults of crystalline thrust sheets, northwestern Wyoming, U.S.A. J. Struct. Geol. 17, 533–547. https://doi.org/10.1016/0191-8141(94)00068-B.

Griffiths, L., Heap, M.J., Wang, F., Daval, D., Gilg, H.A., Baud, P., Schmittbuhl, J., Genter, A., 2016. Geothermal implications for fracture-filling hydrothermal precipitation. Geothermics 64, 235–245. https://doi.org/10.1016/j.geothermics.2016.06.006.

Heap, M.J., Gravley, D.M., Kennedy, B.M., Gilg, H.A., Bertolett, E., Barker, S.L.L., 2020. Quantifying the role of hydrothermal alteration in creating geothermal and epithermal mineral resources: the Ohakuri ignimbrite (Taupō Volcanic Zone, New Zealand). J. Volcanol. Geotherm. Res. 390, 106703. https://doi.org/10.1016/j.jvolgeores.2019.106703.

Hellmann, R., 1994. The albite-water system: Part II. The time-evolution of the stoichiometry of dissolution as a function of pH at 100, 200, and 300°C. Geochim. Cosmochim. Acta 59, 1669–1697. https://doi.org/10.1016/0016-7037(95)00075-B.

Hickman, S., Sibson, R., Bruhn, R., 1995. Mechanical involvement of fluids in faulting. J. Geophys. Res. 100, 12831–12840. https://doi.org/10.1029/94EO01059.

Ikari, M.J., Saffer, D.M., Marone, C., 2009. Frictional and hydrologic properties of clay-rich fault gouge. J. Geophys. Res., Solid Earth 114, 1–18. https://doi.org/10.1029/2008JB006089.

Knauss, K.G., Wolery, T.J., 1986. Dependence of albite dissolution kinetics on pH and time at 25°C and 70°C. Geochim. Cosmochim. Acta 50, 2481–2497. https://doi.org/10.1016/0016-7037(86)90031-1.

Knauss, K.G., Wolery, T.J., 1989. Muscovite dissolution kinetics as a function of pH at elevated temperature. Geochim. Cosmochim. Acta 53, 1493–1501. https://doi.org/10.1016/j.chemgeo.2017.06.003.

Ledingham, P., Cotton, L., Law, R., 2019. The united downs deep geothermal power project. In: Proc. 44th Work. Geotherm. Reserv. Eng., pp. 1–11.

Lee, M.K., Brown, G.C., Webb, P.C., Wheildon, J., Rollin, K.E., 1987. Heat flow, heat production and thermo-tectonic setting in mainland UK. J. Geol. Soc. 144, 35–42. https://doi.org/10.1144/gsjgs.144.1.0035.

Lockner, D.A., Morrow, C., Moore, D., Hickman, S., 2011. Low strength of deep San Andreas fault gouge from SAFOD core. Nature 472, 82–85.

Meredith, P.G., Knight, K.S., Boon, S.A., Wood, I.G., 2001. The microscopic origin of thermal cracking in rocks: an investigation by simultaneous time-of-flight neutron diffraction and acoustic emission monitoring. Geophys. Res. Lett. 28, 2105–2108. https://doi.org/10.1029/2000GL012470.

Mitchell, T.M., Faulkner, D.R., 2008. Experimental measurements of permeability evolution during triaxial compression of initially intact crystalline rocks and implications for fluid flow in fault zones. J. Geophys. Res., Solid Earth 113, 1–16. https://doi.org/10.1029/2008JB005588.

Moore, D.E., Lockner, D.A., Byerlee, J.D., 1994. Reduction of permeability in granite at elevated temperatures. Science 80 (265), 1558–1561. https://doi.org/10.1126/science.265.5178.1558.

Musić, S., Ristić, M., 1988. Adsorption of trace elements or radionuclides on hydrous iron oxides. J. Radioanal. Nucl. Chem. 120, 289–304. https://doi.org/10.1007/BF02037344.

Nagy, K.L., 1995. Dissolution and precipitation kinetics of sheet silicates. In: White, A.F., Brantley, S.L. (Eds.), Chemical Weathering Rates of Silicate Minerals.

Nara, Y., Meredith, P.G., Yoneda, T., Kaneko, K., 2011. Influence of macro-fractures and micro-fractures on permeability and elastic wave velocities in basalt at elevated pressure. Tectonophysics 503, 52–59. https://doi.org/10.1016/j.tecto.2010.09.027.

Oelkers, E.H., Gislason, S.R., Matter, J., 2008. Mineral carbonation of CO2. Elements 4, 333–337. https://doi.org/10.2113/gselements.4.5.333.

Owusu, P.A., Asumadu-Sarkodie, S., 2016. A review of renewable energy sources, sustainability issues and climate change mitigation. Cogent Eng. 3, 1–14. https://doi.org/10.1080/23311916.2016.1167990.

Palandri, J., Kharaka, Y., 2004. A compilation of rate parameters of water-mineral interaction kinetics for application to geochemical modeling, U.S. Geol. Surv. Open File Rep. 2004-1068.

Parkhurst, D.L., Appelo, C.A.J., 2013. Description of Input and Examples for PHREEQC Version 3–A Computer Program for Speciation, Batch-Reaction, One-Dimensional Transport, and Inverse Geochemical Calculations. U.S. Geological Survey.

Paulillo, A., Cotton, L., Law, R., Striolo, A., Lettieri, P., 2020. Geothermal energy in the UK: the life-cycle environmental impacts of electricity production from the United Downs Deep Geothermal Power project. J. Clean. Prod. 249, 119410. https://doi.org/10.1016/J.JCLEPRO.2019.119410.

Pérez-Flores, P., Wang, G., Mitchell, T.M., Meredith, P.G., Nara, Y., Sarkar, V., Cembrano, J., 2017. The effect of offset on fracture permeability of rocks from the Southern Andes Volcanic Zone, Chile. J. Struct. Geol. 104, 142–158. https://doi.org/10.1016/j.jsg.2017.09.015.

Pine, R.J., Batchelor, A.S., 1984. Downward migration of shearing in jointed rock during hydraulic injections. Int. J. Rock Mech. Min. Sci. 21, 249–263. https://doi.org/10.1016/0148-9062(84)92681-0.

Portier, S., Vuataz, F.D., 2010. Developing the ability to model acid-rock interactions and mineral dissolution during the RMA stimulation test performed at the Soultz-sous-Forêts EGS site, France. C. R. Géosci. 342, 668–675. https://doi.org/10.1016/j.crte.2010.04.002.

Richards, H.G., Savage, D., Andrews, J.N., 1992. Granite-water reactions in an experimental Hot Dry Rock geothermal reservoir, Rosemanowes test site, Cornwall, U.K. Appl. Geochem. 7, 193–222. https://doi.org/10.1016/0883-2927(92)90038-5.

Richardson, S.W., Ronald Oxburgh, E., 1978. Heat flow, radiogenic heat production and crustal temperatures in England and Wales. J. Geol. Soc. 135, 323–337. https://doi.org/10.1144/gsjgs.135.3.0323.

Rollin, K.E., 1995. A simple heat-flow quality function and appraisal of heat-flow measurements and heat-flow estimates from the UK Geothermal Catalogue. Tectonophysics 244, 185–196. https://doi.org/10.1016/0040-1951(94)00227-Z.

Sánchez-Roa, C., Bauluz, B., Nieto, F., Abad, I., Jimenéz-Millán, J., Faulkner, D., 2018. Micro- and nano-scale study of deformation induced mineral transformations in Mg-phyllosilicate-rich fault gouges from the Galera Fault Zone (Betic Cordillera, SE Spain). Am. Mineral. 103, 1604–1621. https://doi.org/10.2138/am-2018-6316.

Sánchez-Roa, C., Faulkner, D.R., Boulton, C., Jimenez-Millan, J., Nieto, F., 2017. How phyllosilicate mineral structure affects fault strength in Mg-rich fault systems. Geophys. Res. Lett., 1–11. https://doi.org/10.1002/2017GL073055.

Shail, R.K., Wilkinson, J.J., 1994. Late- to post-Variscan extensional tectonics in South Cornwall. Geosci. South-West Engl. 8, 262–270.

Sibson, R., Robert, F., Poulsen, H., 1988. High-angle reverse faults, fluid-pressure cycling, and mesothermal gold-quartz. Geology 7613. https://doi.org/10.1130/0091-7613(1988)016<0551.

Solberg, P., Lockner, D., Byerlee, J.D., 1980. Hydraulic fracturing in granite under geothermal conditions. Int. J. Rock Mech. Min. Sci. 17, 25–33. https://doi.org/10.1016/0148-9062(80)90003-0.

Townend, J., Zoback, M.D., 2000. How faulting keeps the crust strong. Geology 28, 399–402. https://doi.org/10.1130/0091-7613(2000)028<0399:HFKTCS>2.3.CO;2.

Wang, G., Mitchell, T.M., Meredith, P.G., Nara, Y., Wu, Z., 2016. Influence of gouge thickness and grain size on permeability of macrofractured basalt. J. Geophys. Res., Solid Earth 121, 8472–8487. https://doi.org/10.1002/2016JB013363.

Watanabe, N., Egawa, M., Sakaguchi, K., Ishibashi, T., Tsuchiya, N., 2017. Hydraulic fracturing and permeability enhancement in granite from subcritical/brittle to supercritical/ductile conditions. Geophys. Res. Lett. 44, 5468–5475. https://doi.org/10.1002/2017GL073898.

Wyborn, D., De Graaf, L., Davidson, S., Hann, S., 2005. Development of Australia's first hot fractured rock (HFR) underground heat exchanger, Cooper Basin, South Australia. In: Work. Geotherm. Congr. 2005, pp. 24–29.